APPLICATIONS OF
MODELLING AND SIMULATION
http://arqiipubl.com/ams eISSN 2600-8084 VOL 9, 2025, 199-212

A Combined RSM-FEM Analysis of Electric Field Distribution in a Novel Design of an Inclined-Plane Electrostatic Separator

Abdelkader Nadjem[1*] and Karim Rouagdia[2]

[1]Department of Electrical Engineering, Abbes Laghrour University, 40000, Khenchela, Algeria
[2]Department of Mechanical Engineering, Kasdi Merbah University, 30000, Ouargla, Algeria

[*]Corresponding author: nadjem.abdelkader@univ-khenchela.dz

Submitted 23 January 2025; Revised 14 May 2025; Accepted 16 May 2025; Available online 24 May 2025.

Abstract: The electrostatic separation effectively sorts mixed granular insulators using electrical and mechanical forces. For optimal process performance, particles require a high electric field (E-field) to enhance separation. The present study was aimed at analyzing the E-field distribution within a novel design of an inclined-plane electrostatic separator, which features four flat electrodes and two side openings adjacent to the plane to prevent particle rebound. Simulation experiments were designed to optimize key operating factors, specifically, the width of the horizontal electrodes and both the width and inclination angle of the vertical electrodes using Finite Element Method (FEM) in COMSOL Multiphysics, alongside Response Surface Methodology (RSM) and Central Composite Design (CCD) in JMP statistical software. Maximum, average, and center E-field values were evaluated as performance responses. The quadratic models identified optimal parameters: a horizontal electrode width of 3 cm; vertical electrode width of 1 cm; inclined at 90°, yielding a maximum desirability of 94%. The width of the horizontal electrodes was found to be the most significant factor, contributing over 80% to E-field strength. The correlation between simulated data and model predictions was strong ($R^2 > 0.99$), with prediction errors not exceeding 5.83%. Comparative analysis revealed that our model enhanced E-field parameters by approximately 65% compared to conventional designs.

Keywords: Electric field; Electrostatic separation; Finite element method; Inclined-plane separator; Optimization.

1. INTRODUCTION

Eco-design is becoming increasingly important in response to environmental standards, particularly in the recycling of waste electrical and electronic equipment (WEEE) [1-3]. As recycling efforts expand, there is a growing need for innovative separation technologies to efficiently process industrial waste [4, 5]. The electrostatic separation process is an effective technique that enables the selective sorting of mixed granular insulators using electrical and mechanical forces. For optimal process performance, particles must be subjected to the highest possible electric field (E-field) whereas, in order to prevent particle-electrode collisions, the E-field within the separator has to be high enough. This non-polluting process is significantly affected by the operating parameters of the tribocharging device [6], the properties of the granular materials [7], the relative humidity [8], and the design of the separation device [9]. Optimizing these parameters enhances charging effectiveness and improves separation outcomes.

The inclined-plane electrostatic separator, inspired by traditional free-fall electrostatic separators, has recently been employed for selective sorting of components within granular insulating mixtures [10]. This device consists of an inclined plastic plane and high-voltage electrodes arranged to provide an intense E-field in the separation zone. The electrodes of opposite polarity are typically flat plates arranged parallel to one another and perpendicular to the inclined-plane. By adjusting the inclination angle, this device reduces the gravitational force acting on particles, slowing their movement and enhancing separation [11].

While minimizing mechanical forces is critical for effective separation, it simultaneously necessitates a stronger E-field to effectively deflect particles through electrostatic forces. Consequently, many previous studies have concentrated on enhancing the performance of electrostatic separation devices by increasing E-field strength [12-15]. Proposed solutions include raising electrode voltage and reducing the distance between them. However, these modifications have limitations: excessively high voltage leads to unacceptable power consumption in industrial applications, while very small electrode spacing narrows the separation zone and increases the risk of arcing. Thus, precise control of spacing is necessary to prevent

arcing while maintaining the required field strength. Additionally, these adjustments can adversely affect particle trajectories; a very high E-field may cause particles to rebound upon striking electrodes, decreasing separation efficiency.

In a recent study, Reriballah *et al*. [11] investigated the impact of electrode spacing on the efficiency of separating binary mixtures of polyamide (PA) and acrylonitrile butadiene styrene (ABS) in an inclined configuration. They found that greater spacing allows well-charged ABS particles to avoid colliding with the opposite polarity electrode; however, this increased spacing reduces E-field intensity, which is problematic since poorly charged PA particles require a strong electrostatic field for effective separation. Similar findings indicate that increased electrode spacing leads to decreased E-field strength [16, 17], potentially lowering the separation rate and efficiency. Touhami *et al*. [18] designed a free-fall separator with four vertical cylindrical electrodes instead of two-plate electrodes. Their results demonstrated that this modified configuration reduced particle collisions and increased product purity. However, it generated a less intense E-field compared to the traditional two-plate setup.

Addressing the challenge of increasing E-field strength without considering the potential for particle-electrode collisions can result in undesirable outcomes in electrostatic separation efficiency. Simultaneously enhancing E-field strength while preventing particle-electrode impacts during the separation has emerged as a significant challenge. Given these challenges, modeling and simulation have emerged as widely used tools in scientific research for designing, testing, and optimizing electrostatic separation technologies, enabling performance evaluation without physical models. This approach reduces time and costs compared to constructing and testing multiple physical prototypes. Moreover, virtual prototyping enables a more comprehensive exploration of design factors and their interactions, aiding in the identification of optimal conditions for effective electrostatic separation [19-21].

In this study, Finite Element Method (FEM) simulation coupled with Central Composite Design (CCD) approach-based Response Surface Methodology (RSM) were applied to analyze the E-field distribution and to specify the effect of important operating factors in an inclined-plane electrostatic separator equipped with four flat electrodes, namely the width of horizontal electrodes and the width and inclination angle of vertical electrodes, on key E-field parameters, which are maximum, average, and center E-field. The design of simulation experiments is a very important approach, as it is likely to encourage the use of numerical modeling as an initial step towards designing new electrostatic separators that utilize novel (non-standard) electrode configurations. This approach will also facilitate the identification of optimal electrode settings necessary for constructing physical prototypes applicable in actual electrostatic separation processes. The objective of this research is to provide insights into optimizing separation efficiency in electrostatic separators.

2. METHODS

2.1 Electrostatic separator configuration

The proposed model for simulation experiments in this study is an inclined-plane electrostatic separator equipped with four flat electrodes and two side openings adjacent to the plastic plane. These openings are located between the electrodes of the same polarity (Figure 1). The plastic plane measures 60 cm in length and 10 cm in width, with openings 1 cm wide and extending along the separator. In this design, horizontal auxiliary electrodes are installed on the underside of the inclined plastic plane to enhance the strength of the E-field. This configuration may allow charged particles to easily pass through the side openings, preventing particle rebound and promoting their collection in the designated box, whether before or after colliding with the electrodes.

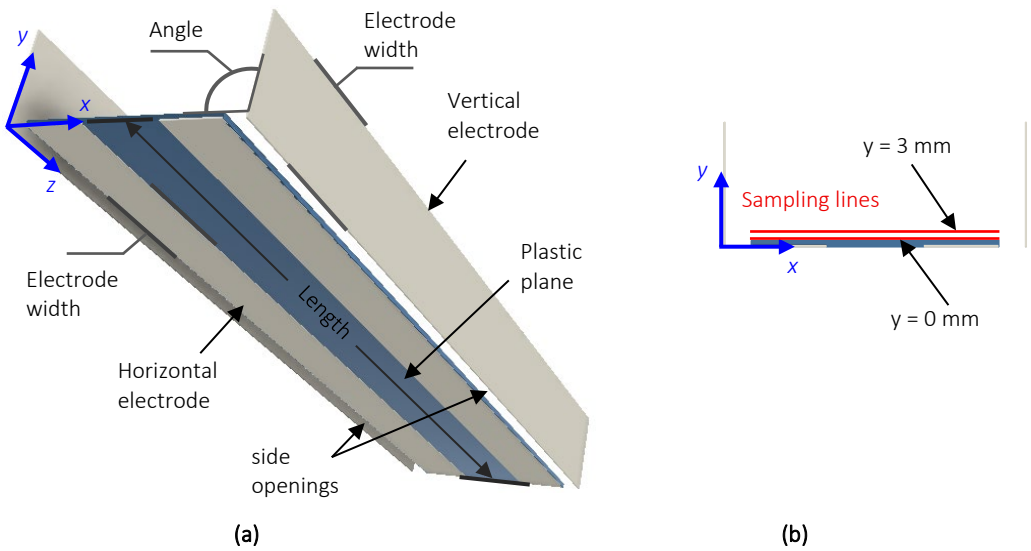

Figure 1. Three-dimensional (3D) numerical model for inclined-plane electrostatic separator with four flat electrodes: (a) problem geometry and (b) E-field intensity sampling lines.

2.2 Design of Experiment (DoE) Methodology

Design of Experiment (DoE) was performed using JMP Pro statistical analysis software (version 14.0.0; SAS Institute Inc, Cary, North Carolina). The objective of the RSM-CCD was to maximize the E-field parameters within the separation zone to effectively separate the charged insulating particles of the mixture. The effect of the independent factors on the E-field parameters was evaluated using a multivariate mathematical model based on RSM. After preliminary simulation experiments, three factors were selected for the CCD: width of horizontal electrodes (X_1), width of vertical electrodes (X_2) and inclination angle of vertical electrodes (X_3). Three responses were evaluated, which represent the E-field parameters: maximum E-field (Y_1), average E-field (Y_2) and E-field at the center (Y_3). The factors studied and their levels are indicated in Table 1, and the responses are listed in Table 2.

The required number of simulated experimental runs (N) was conducted for the selected factors (k) and the number of replicates at the central point (cp) according to the CCD, as determined by the following equation:

$$N = 2^k + 2k + cp \tag{1}$$

Table 1. Studied factors and their levels for the CCD design.

Input parameters	Symbol	Levels		
		low	center	high
Horizontal Electrode Width, HEW (cm)	X_1	0	1.5	3
Vertical Electrode Width, VEW (cm)	X_2	1	3	5
Inclination Angle of Vertical Electrodes, θ (°)	X_3	45	67.5	90

Table 2. Chosen responses for the CCD design.

E- field parameters	Symbol
Maximum E-field, E_{max} (kV/cm)	Y_1
Average E-field, E_{ave} (kV/cm)	Y_2
E-field at the center, E_{center} (kV/cm)	Y_3

2.3 Simulation Model Development

After generating the two-dimensional (2D) models of all studied configurations in SOLIDWORKS 2024 SP1.0, according to the simulated experimental design, they were imported into COMSOL Multiphysics software (version 5.6; COMSOL Inc, Burlington, Massachusetts) to develop numerical simulation using FEM analysis. The effect of the factors studied on the E-field parameters was evaluated using the electrostatics module of COMSOL. Rectangular boundaries were incorporated into each 2D model to represent the surrounding air and define the computation domain, which was essential for accurately simulating the E-field behavior within the specified region of interest. The domains were divided into a large number of finite elements, and the element density for the mesh in critical regions of the model component was increased (extremely fine) to achieve high accuracy of the simulation results. The relative permittivity of air is 1, while the relative permittivity of the polypropylene inclined-plane is 2.3. All the aluminum electrodes have a thickness of 1 mm and an edge radius of 0.2 mm. The DC voltage applied to the electrodes is $U = \pm$ 10 kV in all cases. The behavior of the E-field parameters was simulated on the top surface of this plane.

The values of the responses E_{max} and E_{center} were obtained directly from COMSOL, while E_{ave} was estimated along the x-axis by determining the area under the E-field curve over the interval [a, b] using the trapezoidal rule [22]. Due to symmetry, only half of the area under the curve was calculated; then multiplied by two and divided by the width of the plastic plane (10 cm) to obtain the value of E-field in each 1 cm segment, as expressed in the following equation:

$$E_{ave}(kV/cm) = \frac{2}{(b-a)}\int_a^{(a+b)/2} E(x)\,dx = \frac{\Delta x}{(b-a)}\left[E(x_0) + E\left(x_{(n/2)}\right) + 2\sum_{i=1}^{(n/2)-1} E(x_i)\right] \tag{2}$$

where $E(x)$ is the continuous function defined between $a = 0$ and $b = 10$; n is the number of equal subintervals (with $n = 40$ subintervals); and Δx is the width of each subinterval, which is determined using the following formula:

$$\Delta x = \frac{b-a}{n} \tag{3}$$

The distance x_i at each point on the interval [0, 10] can be calculated using the following formula:

$$x_i = a + i * \Delta x \tag{4}$$

Substituting Equations (3) and (4) into Equation (2), we obtain:

$$E_{ave}(kV/cm) = 0.025 * \left[E(0) + E(20) + 2\sum_{i=1}^{19} E(i * 0.25)\right] \quad (5)$$

2.4 Simulation parameters and Data Analysis

The results from all simulated cases and analysis of the responses obtained from COMSOL were compiled using JMP. Thus, the impacts of all parameters on the models are analyzed and important parameters are determined. A second-order mathematical model was used to evaluate the relationship between the independent factors and their influences on the predicted responses [23, 24], as shown in Equation (6):

$$Y = \beta_0 + \sum_{i=1}^{k} \beta_i X_i + \sum_{i=1}^{k} \beta_{ii} X_i^2 + \sum_{i=1}^{k} \sum_{\substack{j=1 \\ i<j}}^{k} \beta_{ij} X_i X_j + \epsilon \quad (6)$$

Y represents the predicted response, k is the number of independent factors, X_i and X_j are the coded levels for the independent factors, β_0 is an intercept, β_i, β_{ii}, and β_{ij} represent the coefficient values for linear, quadratic, and interaction effects, respectively. Additionally, ϵ represents the error term. The analysis of variance (ANOVA) was also adopted for data processing and statistical analysis of the obtained results, as well as for model validation.

3. RESULTS AND DISCUSSION

3.1 E-field Simulation

In this study, which involved three input factors, each at three levels, the required number of simulated experimental runs (N) was determined according to Equation (1), as follows: $N = 23 + 2X_3 + 1 = 15$. This total number of runs consists of 8 factorial points for assessing main effects and two-way interactions, 6 axial points for evaluating quadratic terms, and 1 central point for assessing model adequacy. The reason for including a single central point is that repeated simulations under similar conditions yield the same results.

In order to generate an intense E-field conducive to efficient particle separation, the geometry of the electrodes must be optimized. The geometrical parameters of the proposed design, including the widths of the electrodes and the inclination angle of the vertical electrodes, can affect the E-field and the electric forces acting on the charged particles. The E-field was simulated for the widths of the vertical and horizontal electrodes, ranging from 1 to 5 cm and 0 to 3 cm, respectively, with the inclination angle of the vertical electrodes varying from 45° to 90°. The horizontal electrodes width of 0 cm was chosen to enable a comparison between two configurations: the conventional configuration without horizontal electrodes, and the proposed configuration with horizontal electrodes, in order to evaluate their impact on performance. Figure 2 presents the variation of the E-field strength as a function of input parameters, based on 15 runs in accordance with the simulated experimental design.

Generally, the areas of highest and lowest E-field strengths can be visually identified through the color intensity in the plot, aiding in understanding of E-field distribution in the models. The intense red color signifies areas where the E-field is concentrated, suggesting that these locations experience the greatest electrical stress and potential effects. Conversely, the intense blue color indicates areas that experience minimal electrical stress and are less affected by the E-field compared to red areas. Figure 2 shows decreasing the distance between the electrodes of opposite polarity - either by increasing the width of horizontal electrodes or by increasing the width of vertical electrodes while reducing their angle of inclination results in an increase in E-field intensity.

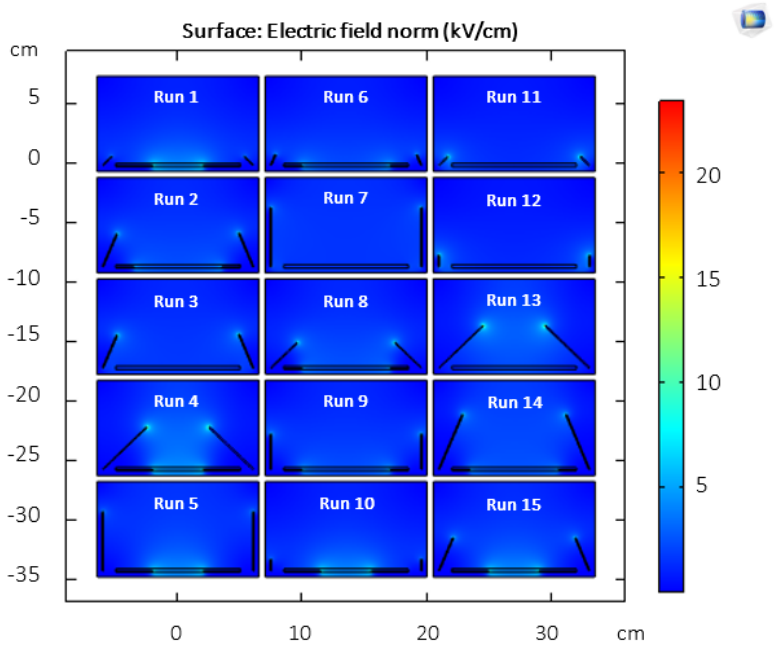

Figure 2. E-field surfaces for the 15 simulated experimental runs: variation of E-field as a function of the input parameters.

3.2 E-field Distribution Analysis

In this investigation, 2D models were designed based on the observation that the E-field values across the planes from $z = 0$ to $z = L$ (along the separator's length) remain markedly consistent. The components of the E-field along the x-axis for the 15 experimental runs are illustrated in Figures 3(a) and 3(b), corresponding to positions $y = 0$ mm and $y = 3$ mm, respectively. A comparative examination of these figures unequivocally demonstrates a discernible decrease in the intensity of the E-field within configurations incorporating horizontal electrodes as the distance from the plane surface increases. Notably, the parameters maintain a consistent influence on the E-field intensity, significantly affecting a substantial portion of the particle volume within the interval spanning $y = 0$ mm to $y = 3$ mm. Consequently, for the purposes of this investigation, the E-field was exclusively analyzed at the plane surface ($y = 0$ mm).

The analysis of the results clearly elucidates the diverse morphologies exhibited by the curves, indicating that changes in the input parameters significantly influence the E-field distribution. Additionally, the results indicate a more intense E-field in the configurations incorporating horizontal electrodes, particularly in the central region where the particles to be separated are introduced. Moreover, regardless of the width and angle of inclination of the vertical electrodes, the highest E-field values on the surface of the plane are observed in regions proximal to the edges of the horizontal electrodes, which have a length of 3 cm. These values range from 5.79 to 6.87 kV/cm, as indicated by the curves represented with solid lines in Figure 3(a). The E-field strength is directly proportional to the voltage applied across the distance between the electrodes [25]. In fact, an augmentation in the length of the horizontal electrodes reduces the distance between them. As the distance decreases, the E-field strength around the edges of the electrodes increases proportionally, enhancing the capacity of the electrodes to affect nearby charged particles.

It is important to note that the E-field intensity can also be enhanced by reducing the distance between the vertical electrodes without the use of horizontal electrodes. However, this adjustment diminishes the separation zone, which is critical for effective particle distribution on the surface. A narrower separation zone can lead to particle accumulation, hindering the separation process by limiting the time available for particles to follow optimal trajectories. Accumulated particles will exert pressure on one another, causing many to fall into the nearest side box. Additionally, particles in the center of the pile may become insulated from the E-field effects. Consequently, this accumulation complicates the separation and the control of particle trajectories.

3.3 Statistical Validation of CCD Data

3.3.1 Design of Simulation Experiments

The efficiency of the electrostatic separation process is significantly influenced by the behavior of the E-field within the device. Key E-field parameters, including E_{max}, E_{ave} and E_{center}, provide information about magnitude and distribution of the E-field. Optimizing these parameters is essential for enhancing separation efficiency. Therefore, the primary objective of this study was to maximize the E-field throughout the entire separation zone by implementing a novel inclined configuration. The results of simulation experiments examining the effects of the studied parameters (HEW, VEW, and θ) on the E-field parameters (E_{max}, E_{ave} and E_{center}) are presented in Table 3. This table includes all 15 simulated experimental runs conducted according to the CCD (Figure 3(a)), along with the parameters studied, their corresponding levels, and the respective responses.

Based on the quadratic Equation (6), an empirical relationship was established between the input variables and the results obtained through the CCD to develop appropriate mathematical models that incorporate interaction terms. The coefficients of each regression polynomial model were derived from multiple regression analysis of the data. Second-order polynomial models were formulated to predict the E-field parameters, which can be expressed in terms of coded factors. In these mathematical models, a positive coefficient indicates a synergistic effect, while a negative coefficient reflects an antagonistic effect. Equations (7), (8), and (9) can be used to predict E_{max}, E_{ave} and E_{center}, respectively, at specified levels of the studied variables.

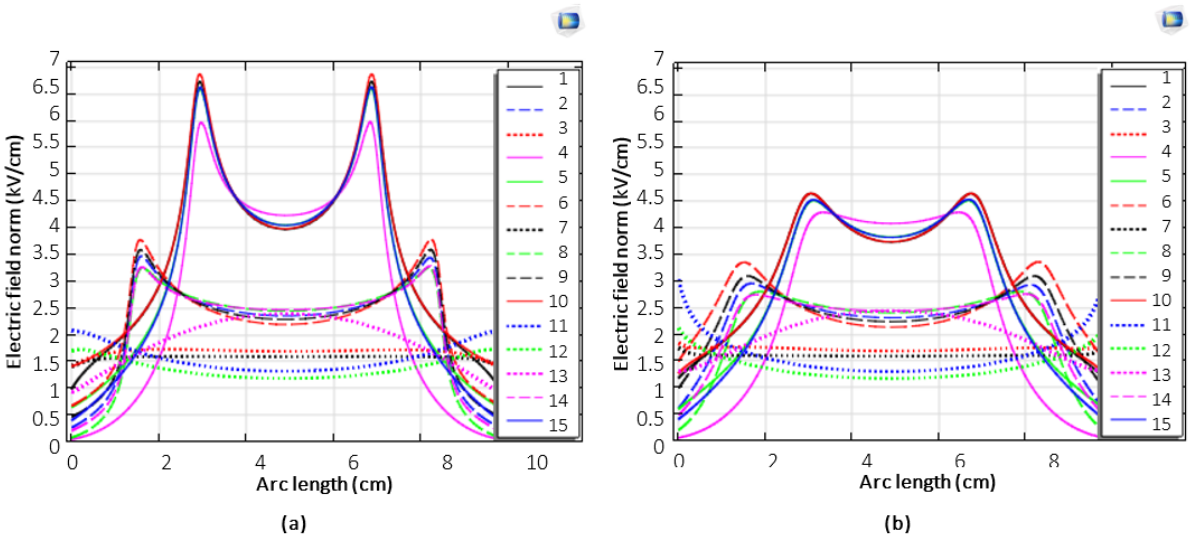

Figure 3. E-field intensity along the sampling lines in Figure 1(b), for the 15 simulated experimental runs: (a) $y = 0$ mm and (b) $y = 3$ mm.

$$Y_1 = 3.4882 + 2.235 * X_1 - 0.041 * X_2 + 0.089 * X_3 + 0.6872 * X_1^2 + 0.0272 * X_2^2 - 0.0727 * X_3^2 - 0.0312 * X_1X_2 + 0.3612 * X_1X_3 - 0.1087 * X_2X_3 \quad (7)$$

$$Y_2 = 2.226 + 0.871 * X_1 - 0.058 * X_2 + 0.038 * X_3 + 0.275 * X_1^2 + 4.684e^{-}17 * X_2^2 - 0.02 * X_3^2 - 0.165 * X_1X_2 + 0.155 * X_1X_3 + 0.015 * X_2X_3 \quad (8)$$

$$Y_3 = 2.3635 + 1.206 * X_1 + 0.217 * X_2 - 0.118 * X_3 + 0.5055 * X_1^2 - 0.0394 * X_2^2 + 0.0055 * X_3^2 - 0.1325 * X_1X_2 + 0.105 * X_1X_3 - 0.1175 * X_2X_3 \quad (9)$$

Table 3. Simulated experimental CCD design along with the responses (Y_1, Y_2 and Y_3) for the specified E-field parameters (E_{max}, E_{ave} and E_{center}).

Run number	Pattern	Studied factors			Responses					
					Simulated (COMSOL)			Predicted (JMP)		
		X_1 HEW (cm)	X_2 VEW (cm)	X_3 θ (°)	Y_1 E_{max} (kV/cm)	Y_2 E_{ave} (kV/cm)	Y_3 E_{center} (kV/cm)	Y_1 E_{max} (kV/cm)	Y_2 E_{ave} (kV/cm)	Y_3 E_{center} (kV/cm)
1	+−−	3	1	45	5.79	3.44	3.9	5.87	3.39	3.85
2	000	1.5	3	67.5	3.47	2.21	2.36	3.48	2.22	2.36
3	a00	0	3	67.5	1.73	1.67	1.69	1.94	1.63	1.66
4	++−	3	5	45	5.97	2.90	4.24	5.95	2.92	4.25
5	+++	3	5	90	6.61	3.39	4.06	6.63	3.33	3.99
6	0a0	1.5	1	67.5	3.77	2.32	2.18	3.55	2.28	2.10
7	−++	0	5	90	1.59	1.57	1.59	1.50	1.61	1.63
8	00a	1.5	3	45	3.25	2.16	2.45	3.32	2.16	2.48
9	00A	1.5	3	90	3.59	2.26	2.29	3.50	2.24	2.25
10	+−+	3	1	90	6.87	3.71	3.99	6.99	3.75	4.06
11	−−−	0	1	45	2.09	1.58	1.32	2.06	1.63	1.38
12	−−+	0	1	90	1.72	1.39	1.19	1.74	1.37	1.17
13	−+−	0	5	45	2.39	1.86	2.39	2.26	1.81	2.31
14	0A0	1.5	5	67.5	3.27	2.14	2.47	3.47	2.16	2.54
15	A00	3	3	67.5	6.63	3.34	4.05	6.41	3.37	4.07

3.3.2 Comparison of Actual and Predicted Values

The correlation plots of actual values (from COMSOL) and predicted values (from JMP) are shown in Figure 4. It can be observed that there is a wide range of E-field parameters depending on the studied variables. By comparing the actual and predicted values, we can determine how well the models approximate the behavior of the E-field as simulated and assess the accuracy and reliability of the predictive models.

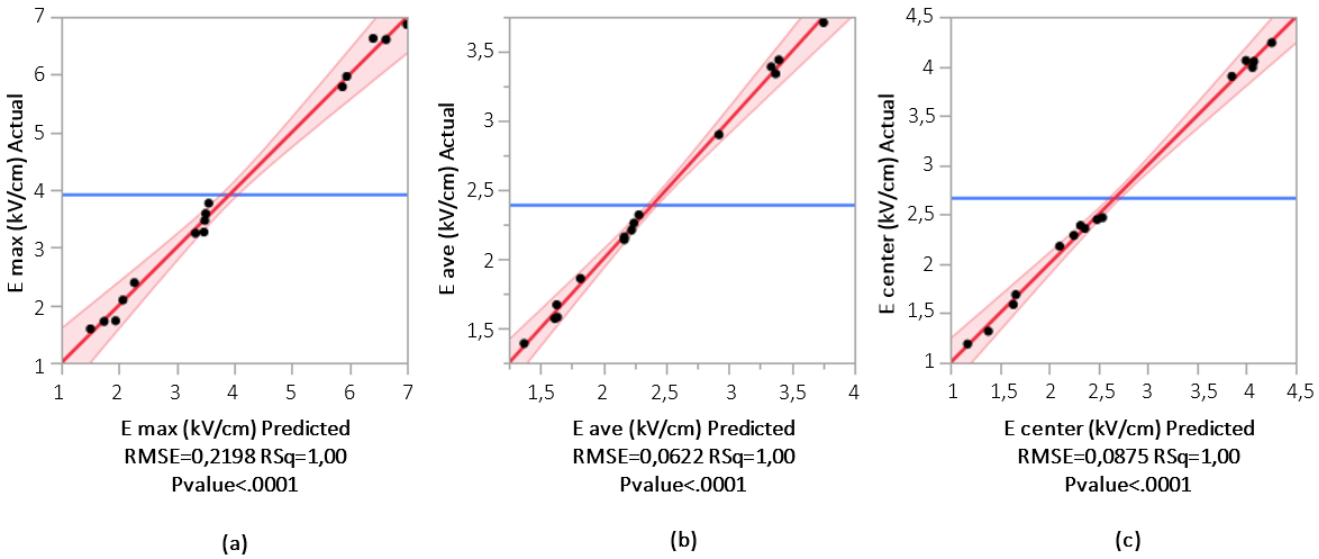

Figure 4. The correlation plots of the actual vs. predicted values of E-field intensity: (a) E_{max}, (b) E_{ave} and (c) E_{center}.

By using Equation (10), the deviation between the simulated experimental values and the predicted values was calculated to determine the percentage error [26].

$$Error\% = \left(\frac{V_{se} - V_p}{V_{se}}\right) \times 100 \quad (10)$$

where Error% is the percentage error, *Vse* is the simulation experimental value and *Vp* is the predicted value. The comparison confirms that the predicted values closely match the actual values, with a low Error% not exceeding 5.83%, indicating that the models are effective and can be used for further analysis or decision-making.

3.3.3 Analysis of Variance (ANOVA)

The ANOVA was performed to validate the quadratic models and assess the significance of the calculated effects [27]. A model is considered statistically significant when the F-ratio exceeds the standard tabulated value and the p-value for the term is less than 0.05 at a 95% confidence level. A smaller *p*-value compared to the significance level (0.05) provides stronger evidence against the null hypothesis, indicating a better fit of the regression model to the data [28]. The ANOVA results, summarized in Table 4, show high F-ratios of 121.1600, 238.2402, and 236.6410 for E_{max}, E_{ave} and E_{center}, respectively, with very low *p*-values of less than 0.0001. These findings indicate a highly significant relationship between the independent and dependent variables. Consequently, the developed models are significant, and the terms have a meaningful effect on the responses.

Table 5 illustrates the values of the statistical significance parameters used by the quadratic models, including the coefficient of determination (R^2), adjusted R^2 ($R^2_{adj.}$), root mean square error (RMSE), and mean response. The regression statistics indicate R^2 values of 0.9954 for E_{max}, 0.9976 for E_{ave}, and 0.9976 for E_{center}. These values demonstrate a strong correlation between the actual and predicted values of the models, suggesting a good fit and accurate prediction of the outcome variable [29, 30]. Furthermore, the similarity between the R^2 and $R^2_{adj.}$ values, with deviation of R^2 value not more than 0.008216 from $R^2_{adj.}$, indicates that the models do not include irrelevant terms (Table 5). According to Bayat *et al*. [31], the difference between R^2 and $R^2_{adj.}$ values should not exceed 0.20 to be in acceptable agreement.

Table 4. Analysis of variance of CCD.

Response	Source	Degree of freedom	Sum of squares	Mean square	F-ratio	Prob. > F
E_{max}	Model	9	52.700313	5.85559	121.1600	<.0001*
	Residual	5	0.241647	0.04833		
	Total	14	52.941960			
E_{ave}	Model	9	8.2850400	0.920560	238.2402	<.0001*
	Residual	5	0.0193200	0.003864		
	Total	14	8.3043600			
E_{center}	Model	9	16.304562	1.81162	236.6410	<.0001*
	Residual	5	0.038278	0.00766		
	Total	14	16.342840			

Table 5. Statistical parameters of CCD.

Source	E_{max}	E_{ave}	E_{center}
R squared (R^2)	0.995436	0.997674	0.997658
Adjusted *R* squared ($R^2_{adj.}$)	0.98722	0.993486	0.993442
R^2 - R^2_{adj}	0.008216	0.004188	0.004216
Root Mean Square Error (RMSE)	0.219839	0.062161	0.087496
Mean of Response	3.916	2.396	2.678
Weighted sums	15	15	15

3.3.4 Effects of the Input Parameters

The coefficient estimates and their main effects on the responses, evaluated through statistical ANOVA analysis, are presented in Table 6. To better highlight the results obtained from the CCD, the percentage effect of each term (Pi) on the responses was calculated using Pareto analysis, as outlined in Equation (11).

$$P_i = \left(\frac{{\beta_i}^2}{\sum_{i=1}^{k} {\beta_i}^2}\right) \times 100 \quad (11)$$

Here, β_i represents the regression coefficient for each term in accordance with coded values, and *k* denotes the number of independent factors.

Table 6. Coefficient estimates from ANOVA analysis.

	E_{max}				E_{ave}				E_{center}			
Term	Estimate	Std Error	t Ratio	Prob>|t|	Estimate	Std Error	t Ratio	Prob>|t|	Estimate	Std Error	t Ratio	Prob>|t|
Intercept	3.4882222	0.11816	29.52	<.0001**	2.226	0.033411	66.63	<.0001**	2.3635556	0.047028	50.26	<.0001**
X_1(0,3)	2.235	0.069519	32.15	<.0001**	0.871	0.019657	44.31	<.0001**	1.206	0.027669	43.59	<.0001**
X_2(1,5)	-0.041	0.069519	-0.59	0.5810^{ns}	-0.058	0.019657	-2.95	0.0319*	0.217	0.027669	7.84	0.0005*
X_3(45,90)	0.089	0.069519	1.28	0.2566^{ns}	0.038	0.019657	1.93	0.1110^{ns}	-0.118	0.027669	-4.26	0.0080*
X_1*X_2	-0.03125	0.077725	-0.40	0.7043^{ns}	-0.165	0.021977	-7.51	0.0007*	-0.1325	0.030935	-4.28	0.0078*
X_1*X_3	0.36125	0.077725	4.65	0.0056*	0.155	0.021977	7.05	0.0009*	0.105	0.030935	3.39	0.0194*
X_2*X_3	-0.10875	0.077725	-1.40	0.2206^{ns}	0.015	0.021977	0.68	0.5252^{ns}	-0.1175	0.030935	-3.80	0.0126*
X_1*X_1	0.6872222	0.137094	5.01	0.0041*	0.275	0.038764	7.09	0.0009*	0.5055556	0.054563	9.27	0.0002*
X_2*X_2	0.0272222	0.137094	0.20	0.8504^{ns}	4.68e-17	0.038764	0.00	1.0000^{ns}	-0.03944	0.054563	-0.72	0.5021^{ns}
X_3*X_3	-0.07277	0.137094	-0.53	0.6182^{ns}	-0.02	0.038764	-0.52	0.6279^{ns}	0.0055556	0.054563	0.10	0.9229^{ns}

**: highly significant ($p < 0.0001$); *: significant ($0.0001 < p < 0.05$); ns: not significant ($p > 0.05$).

To better highlight the results obtained from the CCD, the percentage effect of each term (Pi) on the responses was calculated using Pareto analysis, as outlined in Equation (11).

$$P_i = \left(\frac{{\beta_i}^2}{\sum_{i=1}^{k} {\beta_i}^2}\right) \times 100 \tag{11}$$

Here, β_i represents the regression coefficient for each term in accordance with coded values, and k denotes the number of independent factors. Figure 5 illuminates that the contribution of each variable in the maximization of E-field parameters is different. As shown in Figure 5, among the variables, the width of the horizontal electrodes (X_1) was identified as the most important factor, contributing 88.78%, 85.15%, and 80.13% to E_{max}, E_{ave}, and E_{center}, respectively. In this study, the majority of the terms were identified as statistically significant (Table 6). Specifically, the terms X_1, X_1^2, and X_1*X_3 exhibited significant effects on all responses examined. Conversely, the terms X_2 and X_1*X_2 influenced only the responses E_{ave} and E_{center}. Additionally, the terms X_3 and X_2*X_3 were found to affect only the response E_{center}. The terms X_2^2 and X_3^2 were determined to be statistically insignificant for all responses. The developed second-order polynomial models, illustrated in Equations (12), (13), and (14), predict the responses by considering only the statistically significant terms after omitting the insignificant ones.

$$Y_1 = 3.47 + 2.235 * X_1 + 0.669 * X_1^2 + 0.3612 * X_1X_3 \tag{12}$$

$$Y_2 = 2.218 + 0.871 * X_1 - 0.058 * X_2 + 0.267 * X_1^2 - 0.165 * X_1X_2 + 0.155 * X_1X_3 \tag{13}$$

$$Y_3 = 2.35 + 1.206 * X_1 + 0.217 * X_2 - 0.118 * X_3 + 0.492 * X_1^2 - 0.1325 * X_1X_2 + 0.105 * X_1X_3 - 0.1175 * X_2X_3 \tag{14}$$

The main effects of the studied parameters are represented through the desirability function, as illustrated in Figure 6. This function enables the assessment of the significance of all input variables and facilitates the determination of their optimal settings to achieve the desired process outcome. The HEW variable exhibits a strong positive effect on all responses ($p < 0.0001$), while the VEW variable demonstrates a weak negative effect on E_{ave} ($p = 0.0319$) and a positive effect on E_{center} ($p = 0.0005$). Additionally, the θ variable shows a slight negative effect on E_{center} ($p = 0.0083$).

Among these parameters, HEW stands out as the most significant main effect for all responses. An increase in HEW leads to a significant rise in the responses. This behavior can be explained by the reduction in distance between the electrodes, which allows for a higher total charge to be stored, resulting in a localized intensification of the E-field at the plane surface. The E-field energy becomes strong enough to ionize air for small electrode spacing [32].

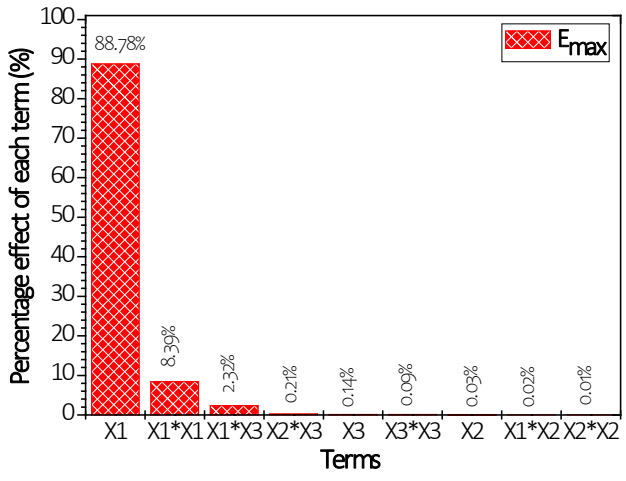

(a)

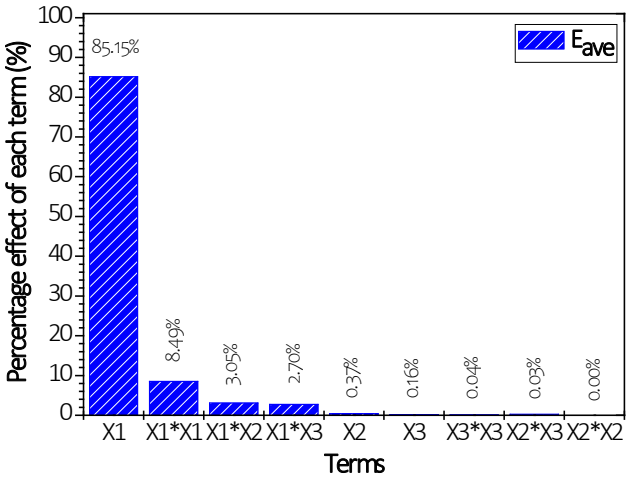

(b)

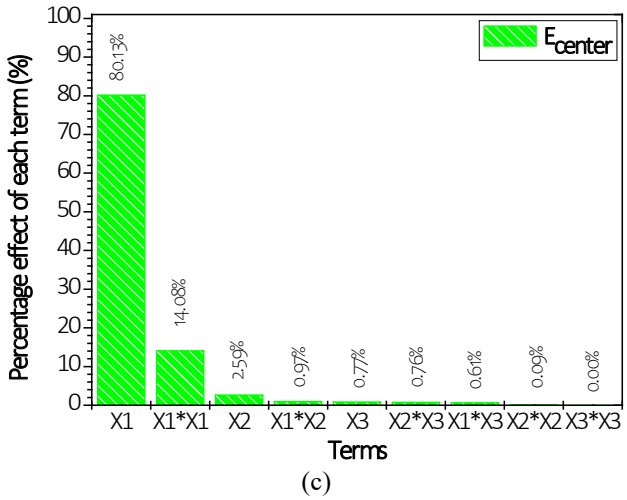

(c)

Figure 5. Pareto chart of main effects of factors on target responses (a) E_{max}, (b) E_{ave}, and (c) E_{center}.

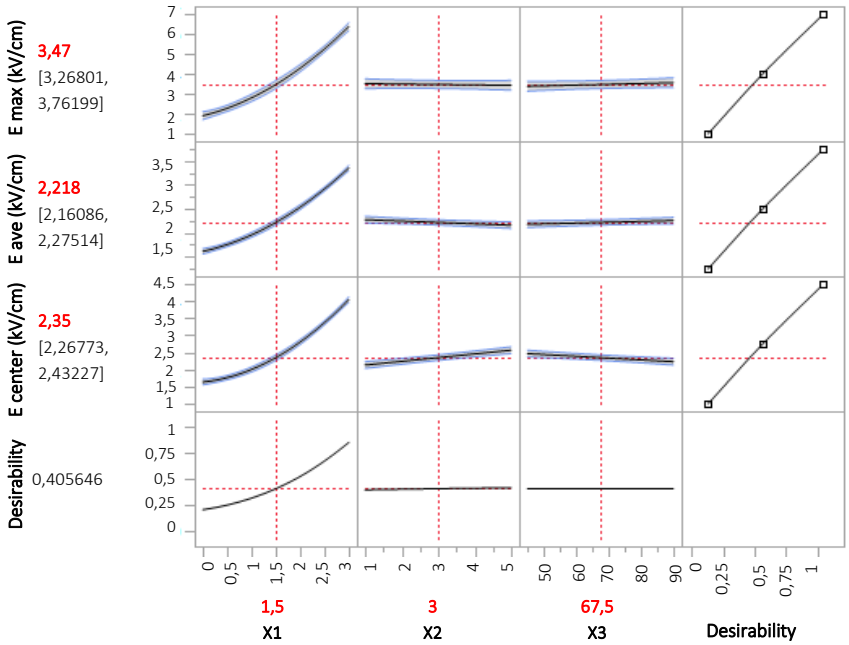

Figure 6. Prediction profiles of the E-field parameters as a function of studied variables.

VEW significantly influences both E_{ave} and E_{center}. As VEW increases, E_{ave} exhibits a slight decrease, while E_{center} increases. This behavior can be attributed to the increasing distance between the plane surface and the upper edges of the electrodes, which leads to a reduction in E-field strength at the surface. The E-field distribution varies considerably between short-width and long-width electrodes. Short-width electrodes exhibit more pronounced edge effects, resulting in higher E-field strengths near the edges. In contrast, as electrode width increases, the effective area for E-field distribution expands, diluting the E-field strength at the surface. With further increases in electrode width, the E-field distribution becomes more uniform across the electrode width, although edge effects still influence the immediate vicinity [33]. Consequently, E_{ave} decreases as VEW increases, indicating that the E-field diminishes at greater distances from the electrode edges. Conversely, as VEW increases, E_{center} also increases. This can be explained by a reduction in electric stress at the edges and a resulting enhancement of a more uniform E-field distribution, thereby strengthening E_{center}.

The parameter θ was found to be significant only for E_{center}. As shown in Figure 6, an increase in θ corresponds to a slight decrease in E_{center}. This effect can be attributed to the improved E-field uniformity resulting from the increase in θ. In fact, higher values of θ enhance the E-field strength in the lateral regions of the surface while concurrently reducing it in the central surface region. This phenomenon highlights the importance of electrode geometry in determining E-field behavior and its implications for device performance [34].

The desirability function, as illustrated in Figure 6, provides a quantitative measure of how well the responses meet the desired criteria, with values ranging from 0 to 1. A desirability value of 0 indicates an undesirable response, while a value of 1 signifies that the response achieves the desired maximum performance for the significant factors [35].

3.4 Synergic Effect of Input Parameters

The proposed models can be effectively utilized to construct 3D response surface plots, supported by the validity of the models as indicated by the statistical parameters presented in Tables 4 and 5. The 3D response surface plots illustrating the influence of the three factors on the parameters of the E-field are shown in Figure 7. Each plot is constructed to highlight the significance of two variables simultaneously while keeping the third variable constant. To fully understand the dynamics at play, the interaction term X_i*X_j is considered significant as long as its corresponding p-value is less than 0.05, even if one of its components (X_i or X_j) is not statistically significant on its own. This indicates that the interaction X_i*X_j may still provide valuable information about the relationship between these variables and the response, which is not captured by the main effect of X_i and X_j [36].

The most significant interaction is observed between HEW and θ, which notably impacts E_{max}, E_{ave}, and E_{center}, with p-values of 0.0056, 0.0009 and 0.0194, respectively (Figures 7(a), 7(b) and 7(c)). An increase in HEW and θ leads to a dramatic rise in all responses. As previously mentioned, an increase in HEW significantly enhances the E-field strength, particularly in the central region of the plane surface, while an increase in θ boosts the E-field strength in the lateral regions. This behavior contributes to an overall enhancement of the E-field across all regions of the surface.

The second interaction between HEW and VEW, as seen in Figures 7(d) and 7(e), also demonstrates significant effects on E_{ave} and E_{center}, with p-values of 0.0007 and 0.0078, respectively. Both responses decrease as the interaction increases. For E_{ave}, the negative interaction effect implies that the positive effect of HEW in E-field intensification is weakened at high levels of VEW when the E-field distribution becomes more uniform. In other words, the beneficial impact of HEW diminishes in the presence of a strong negative influence from VEW (Figure 7(d)). Similarly, the response E_{center} also decreases as the interaction increases, despite the positive main effects of HEW and VEW. When the main effects and interaction effect have opposite signs, it suggests that the effect of one variable on the response is contingent upon the value of the other variable. Precisely, the positive effect of one variable may diminish as the other variable increases [36]. From Equation (13), it is evident that both the main effects of HEW and VEW are positive, while the interaction effect between them is negative. This is further illustrated in Figure 7(e), which demonstrates that the effect of the VEW on E_{center} depends on the value of the HEW. In this context, the positive effect of VEW is attenuated at higher values of HEW. This result can occur due to E-field uniformity and/or saturation effects. As both electrode widths are increased, the E-field distribution may become more uniform, reducing the intensity at the center. In addition, the combined effect of both variables might lead to saturation, where additional increases in either width do not enhance the E-field as expected.

At last, the interaction between VEW and θ significantly affects the E-field strength at the center (E_{center}), with a p-value of 0.0126. Interestingly, while increasing VEW tends to enhance the E-field strength at the center, a concurrent increase in θ leads to a reduction in this strength. Specifically, as θ increases, the effective distance between the electrode's changes, counteracting the positive effects of increasing VEW. This interaction indicates that the combined increase in both variables results in a slight decrease in E_{center}, emphasizing the complexity of their relationship. Figure 7(f) illustrates this interaction, showing how the variations in VEW and θ influence E_{center}.

3.5 Optimization

The optimal settings for the HEW, VEW, and θ variables, based on their respective impacts on the E-field parameters, are presented in Table 7. This table also includes the simulated and predicted values of the responses. From Table 7, it is evident that the predicted values align closely with the simulated experimental data, with a low Error% of 3.93%, indicating a strong agreement between the two sets of results. Notably, the model achieves a maximum desirability of 94.11%, reflecting a very high level of performance.

Table 7. Optimal settings for the studied variables.

Setting	HEW (cm)	VEW (cm)	θ (°)	E-field parameters (kV/cm)						Desirability (%)
				Simulated (COMSOL)			Predicted (JMP)			
				E_{max} (kV/cm)	E_{ave} (kV/cm)	E_{center} (kV/cm)	E_{max} (kV/cm)	E_{ave} (kV/cm)	E_{center} (kV/cm)	
Optimal	3	1	90	6.87	3.71	3.99	7.00 ±0.4	3.75 ±0.11	4.06 ±0.18	94.11

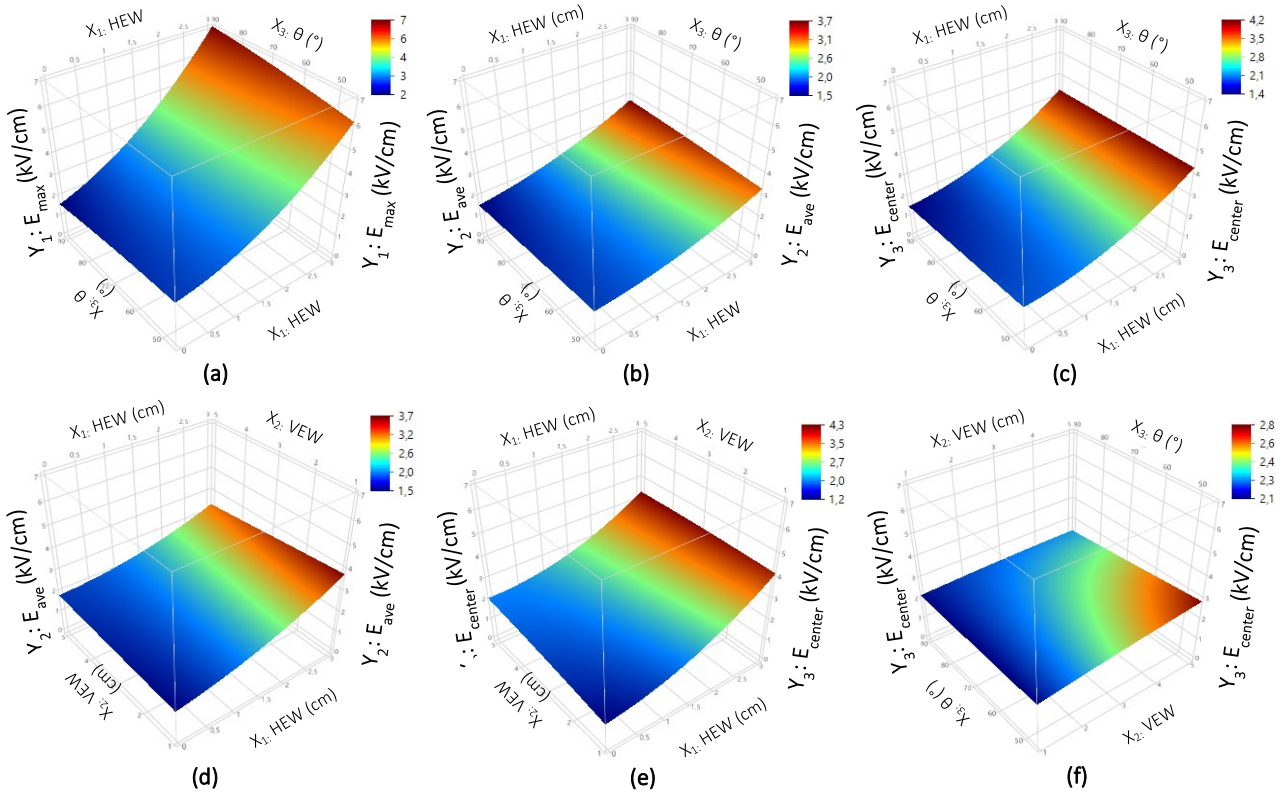

Figure 7. 3D response surface plots of E-field parameters by three factors: Interaction between HEW and VEW: (a) E_{max}, (b) E_{ave} and (c) E_{center}. Interaction between HEW and θ: (d) E_{ave} and (e) E_{center}. Interaction between VEW and θ: (f) E_{center}.

4. COMPARISON BETWEEN THE PROPOSED MODEL AND CONVENTIONAL MODEL

To demonstrate the performance efficiency of the proposed model as an effective separator for enhancing E-field parameters, a comparison with the conventional model is presented. The increase in relative E-field strength resulting from the addition of horizontal electrodes is calculated using the following formula:

$$\Delta E\ \% = \frac{(E_p - E_c) \times 100}{E_c} \tag{15}$$

where E_c and E_p are the optimum values of E-field parameters for models without and with horizontal electrodes, respectively.

Optimal values were attained using vertical electrodes of 5 cm width, inclined at an angle of 45° (run 13), in the absence of horizontal electrodes. In the proposed model, optimal values were achieved by incorporating horizontal electrodes of 3 cm width, along with vertical electrodes of 1 cm width, inclined at an angle of 90° (run 10). This step allowed for a clear estimation of the impact of the horizontal electrodes on the E-field parameters and the overall desirability.

The impact of the horizontal electrodes on E-field distributions is shown in Figure 8. The results demonstrate a significant increase in the intensity of the E-field when horizontal electrodes are incorporated into the device. Figure 9 illustrates the variation in E-field strength increase (ΔE %) for E-field parameters. In all cases, the addition of horizontal electrodes significantly influences the E-field distributions, as illustrated in Figures 2 and 3. This influence is most clearly observed by comparing the optimal E-field parameters of both models.

Without horizontal electrodes, the E-field parameters were E_{max} = 2.39 kV/cm, E_{ave} = 1.86 kV/cm, and E_{center} = 2.39 kV/cm. In contrast, when horizontal electrodes were introduced, these values increased to E_{max} = 6.87 kV/cm, E_{ave} = 3.71 kV/cm, and E_{center} = 3.99 kV/cm (Figure 8), representing increases of 187.45%, 99.46%, and 66.95%, respectively (Figure 9). This enhancement is also notable through the overall desirability value; which increased from 29.43% to 94.11%, demonstrating the high efficiency of the proposed model. Such improvements are likely to lead to better outcomes in the electrostatic separation process.

The optimized design achieves comparable or superior performance at a significantly lower applied voltage (6 kV vs. 10 kV in the conventional configuration), yielding a 40% reduction in power consumption. Moreover, the proposed design demonstrates enhanced E-field parameters, with higher maximum (E_{max} = 4.12 kV/cm vs. 2.39 kV/cm) and average (E_{ave} = 2.22 kV/cm vs. 1.86 kV/cm) field strength while maintaining identical central field strength (E_{center} = 2.39 kV/cm for both configurations).

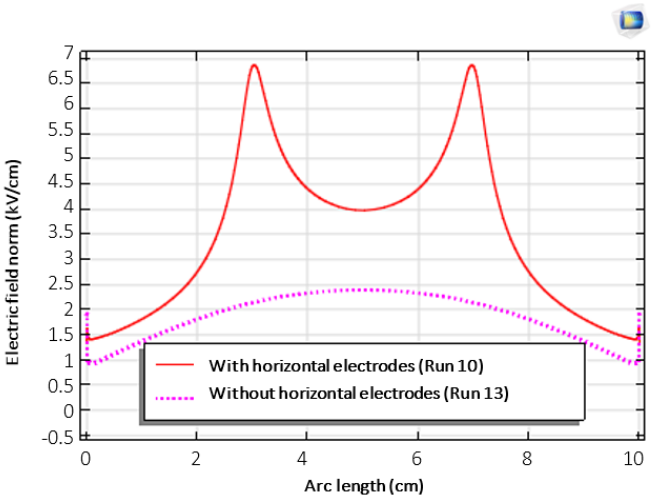

Figure 8. Influence of the horizontal electrodes on E-field distributions.

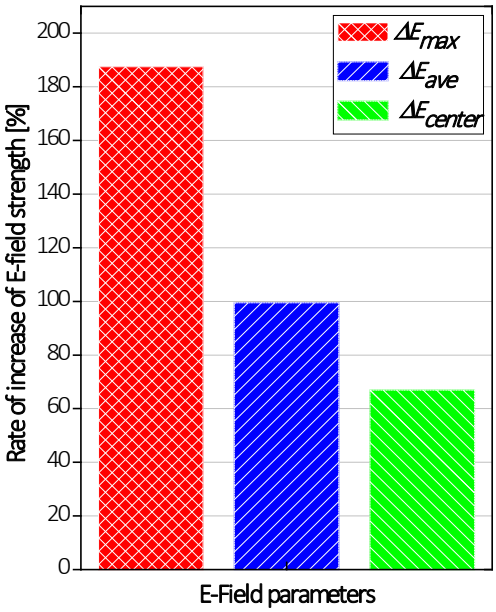

Figure 9. Variation rates of E-field parameters.

5. CONCLUSION

This study focuses on modelling and simulation of E-field distribution in a new inclined-plane electrostatic separator design using FEM to calculate key E-field parameters, including E_{max}, E_{ave}, and E_{center}. After generating the 2D models, we investigated the individual and interaction effects of three geometrical parameters of the proposed design: the width of the horizontal electrodes (HEW), the width of the vertical electrodes (VEW), and the inclination angle of the vertical electrodes (θ) on the E-field parameters. This was achieved through the design and analysis of simulation experiments supported by the RSM-CCD approach. It was found that HEW is the most significant factor affecting the E-field parameters, with its percentage effect exceeding 80% of the total effect. The predicted E-field parameters showed good agreement with the simulation experimental results, with $R^2 > 0.99$ and error percentages $\leq 5.83\%$. Based on RSM plots, the maximum values of E-field parameters are obtained under the following optimum conditions: HEW = 3 cm, VEW = 1 cm and $\theta = 90°$. The proposed model significantly enhances the E-field parameters compared to the conventional model, with increases in E_{max}, E_{ave}, and E_{center} of 187.45%, 99.46%, and 66.95%, respectively, demonstrating its high efficiency. This optimization is crucial for plastic recycling applications in electro-separator devices, where the E-field intensity directly influences performance metrics such as electric forces and particle trajectories. Such improvements are likely to lead to better outcomes in the electrostatic separation process. The integrated approach of using JMP and COMSOL for the design of simulation experiments enhances the research process, making it more efficient and insightful. A key direction for future research will involve experimental validation, including design, fabrication, and prototype testing. This phase will rigorously assess actual separation performance in real-world applications to validate the theoretical and computational findings. Key performance metrics, such as recovery rate, purity, and energy consumption, will be quantitatively evaluated. Additionally, the experimental results will provide critical insights into potential scalability, operational challenges, and optimization opportunities. By bridging the gap between computational predictions and practical implementation, this work will strengthen the technological feasibility and industrial applicability of the proposed separation system.

ACKNOWLEDGEMENT AND FUNDING

The authors receive no financial support for the research, authorship, and publication of this article.

DECLARATION OF CONFLICTING INTERESTS

The authors declare no potential conflicts of interest with respect to the research and publication of this article.

REFERENCES

[1] C. Fenwick, K. Mayers, J. Lee and R. Murphy, Recycling plastics from e-waste: Implications for effective eco-design, *Journal of Industrial Ecology*, 27(5), 2023, 1370-1388.

[2] K. S. Khor, T. Ramayah and H. R. P. Fouladgaran, Managing eco-design for reverse logistics, *International Journal of Environment and Waste Management*, 26(2), 2020, 125-146.

[3] P. Cicconi, Eco-design and eco-materials: An interactive and collaborative approach, *Sustainable Materials and Technologies*, 23, 2020, e00135.

[4] G. Chauhan, P. R. Jadhao, K. K. Pant and K. D. P. Nigam, Novel technologies and conventional processes for recovery of metals from waste electrical and electronic equipment: Challenges & opportunities – A review, *Journal of Environmental Chemical Engineering*, 6(1), 2018, 1288-1304.

[5] Z. Wang, N. J. Miles, T. Wu, F. Gu and P. Hall, Recycling oriented vertical vibratory separation of copper and polypropylene particles, *Powder Technology*, 301, 2016, 694-700.
[6] A. Benabboun, A. Tilmatine, Y. Brahami, S. E. Bendimerad, M. Miloudi and K. Medles, Experimental investigation of electrostatic separators of plastic particles using different charging devices, *Separation Science and Technology*, 49(3), 2014, 464-468.
[7] A. Nadjem, M. Kachi, F. Bekkara, K. Medles, T. Zeghloul and L. Dascalescu, Triboelectrification of granular insulating materials as affected by dielectric barrier discharge (DBD) treatment, *Journal of Electrostatics*, 86, 2017, 18-23.
[8] S. K. Mohanta, B. Rout, R. K. Dwari, P. S. R. Reddy and B. K. Mishra, Tribo-electrostatic separation of high ash coking coal washery rejects: Effect of moisture on separation efficiency, *Powder Technology*, 294, 2016, 292-300.
[9] M. Miloudi, K. Medles, A. Tilmatine, A. Bendaoud and L. Dascalescu, Optimization of belt-type electrostatic separation of triboaerodynamically charged granular plastic mixtures, *IEEE Transactions on Industry Applications*, 49(4), 2013, 1781-1786.
[10] A. Nadjem, M. Kachi, K. Rouagdia and M. Remadnia, Experimental study of an inclined-plane electrostatic separator, *Proceedings of the Third International Symposium on Materials and Sustainable Development*, 2018, 439-450.
[11] H. Reriballah, W. Aksa, M. F. Boukhoulda, S. Touhami, K. Medles and A. Tilmatine, realization and optimization of a new inclined plane electro-separator, *2019 International Conference on Advanced Electrical Engineering (ICAEE)*, 2019, 1-6.
[12] M. Xue, G. Yan, J. Li and Z. Xu, Electrostatic separation for recycling conductors, semiconductors, and nonconductors from electronic waste, *Environmental Science & Technology*, 46(19), 2012, 10556-10563.
[13] H. Louati, A. Tilmatine, R. Ouiddir, A. Alibida and N. Zouzou, New separation technique of metal/polymer granular materials using an electrostatic sorting device, *Journal of Electrostatics*, 103, 2020, 103410.
[14] M. Miloudi, L. Dascalescu, J. Li, S. El-Mossouess and K. Medles, Tribo-aero-electrostatic separator for coarse granular insulating materials, *IEEE Transactions on Dielectrics and Electrical Insulation*, 20(5), 2013, 1510-1515.
[15] J. Li and L. Dascalescu, Newly-patented technical solutions for improving the tribo-electrostatic separation of mixed granular solids, *Recent Patents on Engineering*, 6(2), 2012, 104-115.
[16] H. Zhang, G. Pan and H. Zheng, Optimization of two-stage high-voltage electrostatic separation parameters for retired passenger vehicle plastics by response surface methodology, *Materiale Plastice*, 59(4), 2022, 109.
[17] M. Maammar, T. Zeghloul, W. Aksa, S. Touhami, I. Achouri and L. Dascalescu, Factors that influence the trajectories of charged insulating particles in roll-type electrostatic separators, *Journal of Electrostatics*, 115, 2022, 103672.
[18] S. Touhami, W. Aksa, M. Maammar, T. Zeghloul, K. Medles and L. Dascalescu, Numerical simulation of the behavior of insulating particles in a free fall tribo-electrostatic separator with four vertical cylindrical electrodes, *Journal of Electrostatics*, 97, 2019, 8-14.
[19] M. Xue and Z. Xu, Computer simulation of the pneumatic separator in the pneumatic- electrostatic separation system for recycling waste printed circuit boards with electronic components, *Environmental Science & Technology*, 47(9), 2013, 4598-4604.
[20] P. M. Ireland, Modelling dense particle streams during free-fall electrostatic separation, *Powder Technology*, 434, 2024, 119290.
[21] J. Li, H. Lu, S. Liu and Z. Xu, Optimizing the operating parameters of corona electrostatic separation for recycling waste scraped printed circuit boards by computer simulation of electric field, *Journal of Hazardous Materials*, 153(1-2), 2008, 269-275.
[22] A. N. Tuah, A. B. Ibrahim, S. Dzulkifly, F. Mohammad Yusof, R. Awang Nor and R. Ariffin, Analysis of the area under a curve (AUC) using C-programming: Trapezium and Simpson rules techniques, *Journal of ICT in Education*, 9(1), 2022, 143-153.
[23] D. Baş and I. H. Boyaci, Modeling and optimization I: Usability of response surface methodology, *Journal of Food Engineering*, 78(3), 2007, 836-845.
[24] N. Kadous, F. Miloua, F. Z. Rahou and A. Tilmatine, Optimisation of the electrostatic separation process using the design of experiments methodology, *Materials Technology*, 20(3), 2005, 156-160.
[25] A. Bendaoud, A. Tilmatine, K. Medles, M. Rahli, M. Huzau and L. Dascalescu, Characterization of dual corona-electrostatic electrodes for electrostatic processes applications, *IEEE Transactions on Industry Applications*, 44(3), 2008, 692-698.
[26] Y. T. Chung, L. Y. Ng and A. W. Mohammad, Sulfonated-polysulfone membrane surface modification by employing methacrylic acid through UV-grafting: Optimization through response surface methodology approach, *Journal of Industrial and Engineering Chemistry*, 20(4), 2014, 1549-1557.
[27] S. F. Sawyer, Analysis of variance: The fundamental concepts, *Journal of Manual & Manipulative Therapy*, 17(2), 2009, 27E-38E.
[28] D. Szucs and J. P. A. Ioannidis, When null hypothesis significance testing is unsuitable for research: A reassessment, *Frontiers in Human Neuroscience*, 11, 2017, 390.
[29] D. Zhang, A coefficient of determination for generalized linear models, *The American Statistician*, 71(4), 2017, 310-316.
[30] C. L. Cheng, Shalabh and G. Garg, Coefficient of determination for multiple measurement error models, *Journal of Multivariate Analysis*, 126, 2014, 137-152.
[31] A. Bayat, H. R. Mahdavi, M. Kazemimoghaddam and T. Mohammadi, Preparation and characterization of γ-alumina ceramic ultrafiltration membranes for pretreatment of oily wastewater, *Desalination and Water Treatment*, 57(51), 2016, 24322-24332.
[32] L. Zigan, Overview of electric field applications in energy and process engineering, *Energies*, 11(6), 2018, 1361

[33] V. K. Gandi, R. Verma, M. Warrier and A. Sharma, Effect of electrode profile and polarity on performance of pressurized sparkgap switch, *Plasma*, 5(1), 2022, 130-145.
[34] M. Maammar, S. Touhami, M. Rezoug, K. Daioui, L. Dascalescu and K. Medles, Experimental study and numerical simulation of particles trajectories in a flexible-electrode-type electrostatic separator, *Journal of Physics: Conference Series*, 2702(1), 2024, 012018.
[35] D. Singh and P. V. Rao, A surface roughness prediction model for hard turning process, *The International Journal of Advanced Manufacturing Technology*, 32, 2007, 1115-1124.
[36] Statistics By Jim, *Understanding Interaction Effects in Statistics*. https://statisticsbyjim.com/regression/interaction-effects/, 2024 (accessed 13.12.2024).